Renewable Energy 256 (2026) 123943

Contents lists available at ScienceDirect

Renewable Energy

journal homepage: www.elsevier.com/locate/renene

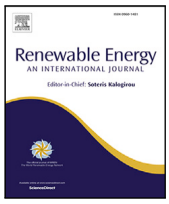

A hierarchical Bayesian spatio-temporal model for estimating solar radiation from sunshine duration records

Santiago Beguería [a],*, Sergio M. Vicente-Serrano [b], José Manuel Gutiérrez-Llorente [c], Swen Brands [c], Marcos Gil-Guallar [a], Alejandro Royo-Aranda [b], María del Mar Rondón-Velasco [a], Antonio Torralba-Gallego [b], Yolanda Luna [d], Ana Morata [d]

[a] Estación Experimental de Aula Dei–Consejo Superior de Investigaciones Científicas (EEAD-CSIC), Zaragoza, Spain
[b] Instituto Pirenaico de Ecología–Consejo Superior de Investigaciones Científicas (IPE-CSIC), Zaragoza, Spain
[c] Instituto de Física de Cantabria (CSIC-UC), Santander, Spain
[d] Agencia Estatal de Meteorología (AEMET), Madrid, Spain

ARTICLE INFO

Keywords:
Solar radiation
Sunshine duration
Angström–Prescott model
Hierarchical Bayesian modelling
Spatio-temporal analysis
Integrated nested Laplace approximation
Spain

ABSTRACT

Estimating surface solar radiation is essential for applications in climatology, agriculture, and renewable energy, yet direct radiation measurements are often sparse or unavailable. This study presents a hierarchical Bayesian spatio-temporal model for estimating daily solar radiation from sunshine duration records, using an extended version of the Angström–Prescott (A–P) empirical relationship. The model incorporates fixed effects, elevation-dependent covariates, spatially and temporally structured latent fields, and unstructured random effects, estimated using the Integrated Nested Laplace Approximation (INLA) and the Stochastic Partial Differential Equation (SPDE) approach. Applied to a comprehensive observational dataset covering mainland Spain (1973–2024), the model reveals coherent spatial and seasonal patterns in the A–P coefficients, including a strong altitude effect on the slope parameter and opposing seasonal cycles for the intercept and slope. Validation against observed radiation data shows excellent agreement for most aspects of the distribution, with remaining discrepancies explained by known limitations in the sunshine duration measurements, particularly under overcast conditions. Long-term temporal trends in the slope suggest changes in atmospheric transmissivity, potentially linked to air quality and aerosol dynamics. The proposed framework provides a flexible, computationally efficient, and physically interpretable tool for reconstructing solar radiation fields in data-scarce regions, offering broad relevance for environmental and climate-related applications.

1. Introduction

Solar radiation incident at the Earth's surface is a fundamental driver of the planet's energy balance and climate system [1]. Of the roughly 340 $W\,m^{-2}$ of solar radiation that reaches the Earth, about 240 $W\,m^{-2}$ is absorbed. This absorbed sunlight fuels essential processes such as photosynthesis, drives evaporation, melts snow and ice, and warms the entire Earth system. The accumulation of energy within the Earth system, quantified through changes in the global energy inventory, is now established as a robust measure of the rate of global climate change. Beyond its role in the overall energy balance, solar irradiance is also a critical forcing quantity for heat fluxes, which in turn drive atmospheric motion and circulation patterns. Therefore, understanding the complexities of the Earth's energy balance and the trajectory of climate change necessitates precise measurements of solar radiation reaching the Earth's surface [2].

Accurate measurements or estimates are essential not only for meteorological and climatological research, but also for a wide range of practical applications. These include the design and optimisation of solar energy systems [3], hydrological and crop modelling [4], irrigation scheduling, and the management of water resources under changing climatic conditions. In particular, surface solar radiation plays a central role in the estimation of evapotranspiration (ET), a key component of the hydrological cycle and a major determinant of agricultural water demand [5].

Solar radiation is not a constant entity; its intensity varies significantly depending on factors such as the season, the time of day, and the geographical latitude, and on atmospheric conditions including the presence of clouds and aerosols [6]. Furthermore, observational records indicate temporal variability, with periods of decline (dimming) followed by partial recovery (brightening) in the amount of

* Corresponding author.
E-mail address: santiago.begueria@csic.es (S. Beguería).

https://doi.org/10.1016/j.renene.2025.123943
Received 17 May 2025; Received in revised form 26 June 2025; Accepted 5 July 2025
Available online 6 August 2025

solar radiation reaching the surface over the past several decades [7]. This inherent variability underscores the inadequacy of relying on a single global average for solar radiation and highlights the need for detailed, location-specific, and time-sensitive measurements to accurately represent the energy input to the Earth system.

However, direct measurements of surface solar radiation are often sparse due to high equipment costs and maintenance demands. In contrast, sunshine duration records — defined as the time during which direct solar radiation exceeds a certain threshold — are more densely distributed geographically and often span longer historical periods. Utilising sunshine duration data to estimate solar radiation presents an opportunity to obtain high-quality solar resource information in locations and periods lacking direct radiation measurements, offering an opportunity to undertake long-term studies over large regions [8].

The Ångström–Prescott (A–P) model remains a foundational empirical approach to estimating solar radiation from sunshine duration [9]. This model linearly relates the ratio of observed to extraterrestrial radiation (clearness index) to the ratio of observed sunshine duration to maximum possible sunshine duration or day length [10]. Due to its simplicity, interpretability, and general effectiveness, the A–P equation has become widely adopted globally. In the absence of local solar radiation data, general recommendations suggest using coefficients derived from nearby or climatically similar regions or even global values, potentially compromising accuracy [11].

Nevertheless, sunshine duration alone does not entirely explain radiation variability, as geographic and day-to-day fluctuations influenced by random factors such as atmospheric turbidity, humidity, cloud optical properties, and aerosol concentrations significantly impact solar irradiance. Thus, there is a need for flexible estimation frameworks capable of capturing global spatial patterns, seasonal cycles, and subtle daily variations influenced by these random atmospheric factors [12]. A comprehensive literature review reveals a recurring emphasis on "site-specific" or "local calibration" across research from Poland [13], Iran [14], Chad [15], Zimbabwe [16], Nepal [17], India [18], West Africa [19], Brazil [20], China [21] and Spain [22]. This underscores the need for regional studies to refine ground-level estimations.

The vast majority of studies have relied on linear regression techniques, making them the *de facto* standard for estimating solar radiation. More recently, a handful of investigations have explored machine learning methods [23]. While these approaches can capture non-linear relationships and, in some cases, yield higher accuracy, they often function as "black boxes", demand large training datasets, and lack flexibility for incremental updates without full retraining. In contrast, hierarchical Bayesian spatio-temporal models have emerged as a compelling alternative because they explicitly quantify uncertainty, accommodate multi-level spatial and temporal variability, and allow parameters to be updated as new observations arrive [24]. Although several studies have applied Bayesian methods to solar radiation estimation, highlighting their robustness under data scarcity and their ability to model structured spatial or temporal patterns, few have specifically employed this framework to fit Angström–Prescott coefficients [25].

The objective of this study is to estimate global solar radiation using sunshine duration records within a hierarchical Bayesian spatio-temporal modelling framework, on the Spanish mainland. Several previous studies examined the estimation and analysis of global solar radiation in Spain using sunshine duration records and empirical modelling approaches. Thus, Almorox and Hontoria [26] evaluated linear and polynomial regression models across 16 meteorological stations, highlighting the practical advantage of simpler linear models despite marginally improved performance from more complex alternatives. Almorox et al. [27] refined this approach by calculating monthly-specific Angström–Prescott (A–P) coefficients in Toledo, emphasising the accuracy gained by accounting for seasonal atmospheric variability. Sanchez-Lorenzo et al. [8] constructed a homogenised dataset from 50 Spanish stations (1950–2011), identifying distinct phases of global dimming and subsequent brightening, linked to aerosol concentrations and cloud cover. Similarly, Rom00E1n et al. [28] reconstructed daily solar radiation over six decades using sunshine duration records, revealing spatial and temporal patterns, including episodes of brightening and dimming. Antón et al. [29] extended the temporal scope by analysing historical records from 1887 to 1950 in Madrid, differentiating between all-sky and cloud-free conditions to isolate the role of aerosols and clouds. In a broader methodological contribution, Manzano et al. [30] proposed a unified calibration of the A–P equation across 37 Spanish stations using data from 1981 to 2010. Finally, Almorox et al. [22] reviewed the effects of total solar irradiance variability on empirical models, recommending its consideration to enhance model robustness.

Our study offers several contributions beyond these earlier efforts. First, we utilise the most comprehensive dataset assembled to date, incorporating data from more than 250 meteorological stations spanning the entirety of mainland Spain and covering an extended time period from 1961 to 2024. This temporal coverage includes recent decades that are underrepresented in previous analyses. Second, we implement a hierarchical Bayesian spatio-temporal modelling framework, which allows us to simultaneously estimate spatially and seasonally varying A–P coefficients while accounting for both structured and unstructured sources of variability. This approach provides a statistically robust uncertainty quantification and offers detailed insight into spatial, seasonal, and long-term patterns in atmospheric transmissivity, making it a robust and scalable tool for solar radiation estimation in both retrospective and predictive applications. It also enhances the physical interpretability, predictive accuracy, and generalisability of empirical solar radiation models, offering a flexible solution for data-scarce regions and for retrospective analysis where direct radiation records are unavailable.

2. Data and methods

The diagram in Fig. 1 provides an overview of the full workflow, showing how raw measurements, deterministic computations, and statistical components are combined to estimate relative solar radiation, R^*. The red nodes at the top (latitude, day of year, observed sunshine duration n, observed solar radiation H, and altitude) represent direct field measurements at each station. From latitude and day of year, we deterministically compute extraterrestrial radiation H_0 and the theoretical maximum sunshine duration N. These, together with observed sunshine n, yield the relative sunshine duration n^*. Similarly, observed radiation divided by extraterrestrial radiation yields relative solar radiation R^*.

Solid arrows denote purely deterministic transformations, based on astronomical geometry and physical laws, while dashed arrows indicate stochastic relationships that are estimated from the data. These stochastic relationships are encapsulated within the hierarchical Bayesian model (HBM), represented by the diamond-shaped node. The HBM jointly models the effects of n^*, altitude, and spatio-temporal structure to estimate latent relative solar radiation $\hat{R}^*$. This estimate can be converted into absolute solar radiation $\hat{H}$ via the known quantity H_0. A detailed, step-by-step description follows.

2.1. Radiation and sunshine duration data

This study relies on observational data from the National Climate Data Bank of the Spanish Meteorological Agency (AEMET). Two key variables were used: daily sunshine duration and daily incoming solar radiation. The data span a 51-year period, from January 1, 1973, to December 31, 2024.

The dataset used in this study includes 1,154,725 daily records of sunshine duration from 258 meteorological observatories, and 491,700 records of global solar radiation from 78 observatories across Spain. Of these, 68 stations provided simultaneous measurements of both variables, allowing for direct calibration of empirical models relating sunshine duration and solar radiation.

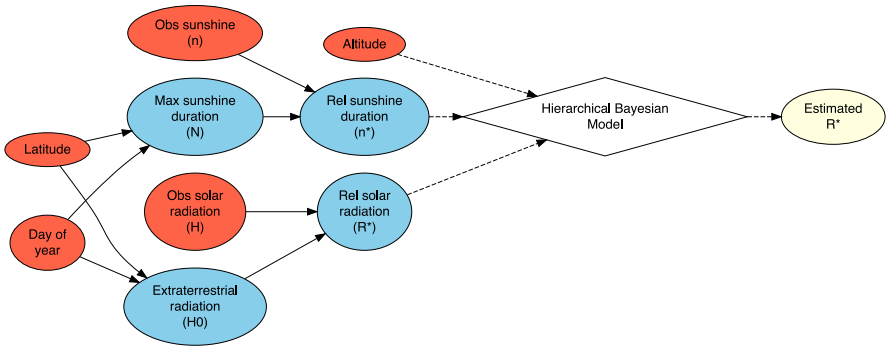

Fig. 1. Directed acyclic graph summarising our methodological framework. Red nodes represent measured inputs, while blue nodes denote deterministic, computed quantities. Yellow nodes correspond to stochastic components resulting from the hierarchical Bayesian model. Solid arrows indicate purely deterministic transformations, while dashed arrows indicate relationships that are statistically estimated.

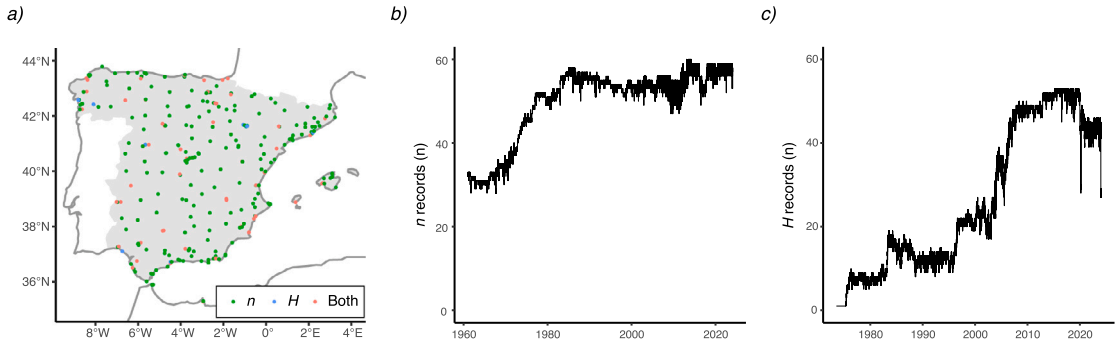

Fig. 2. Availability of solar radiation (H) and sunshine duration (n) records in mainland Spain during 1961–2024: (a) spatial distribution of observatories; (b) temporal distribution of sunshine duration records; (c) temporal distribution of solar radiation records.

Sunshine duration was recorded using Campbell–Stokes heliographs. Global solar radiation was measured using Kipp & Zonen pyranometers, which were regularly calibrated at the National Radiometric Centre (Centro de Referencia Radiométrica, CRN) following World Meteorological Organization (WMO) protocols.

The spatial distribution of the observatories provides regular coverage of the study area, as shown in Fig. 2a. The temporal distribution of data availability (Figs. 2b and c) reveals a marked increase in data availability in the last two decades of the period, while earlier decades show a progressive decline in observational density. It is also noteworthy that sunshine duration records are not only more numerous overall but also denser during the earlier decades compared to solar radiation measurements.

This discrepancy in data density between the two variables highlights the potential for leveraging the more abundant sunshine duration data to estimate solar radiation where direct measurements are unavailable.

2.2. Calculation of relative radiation and sunshine duration

The foundational method for estimating surface radiation H (MJ m^{-2} d^{-1}) from observed relative sunshine duration n/N (adimensional) is the A–P model, an empirical linear relationship expressed as:

$$H = \left(a + b\frac{n}{N}\right) H_0, \quad \text{subject to} \quad a \geq 0, \quad b \geq 0, \quad a + b \leq 1 \tag{1}$$

where H_0 is the extraterrestrial (top of the atmosphere) radiation (MJ m^{-2} d^{-1}), n is the recorded sunshine duration (h), N is the maximum possible sunshine duration or day length (h), and a and b are empirical coefficients.

Coefficients a and b can be physically interpreted as follows: a expresses the fraction of extraterrestrial radiation received at the Earth's surface under completely overcast conditions (when sunshine duration is zero, $n = 0$), that is it indicates the portion of solar energy transmitted through the atmosphere purely due to diffuse radiation (under no direct sunlight); and $a + b$ is the fraction of extraterrestrial radiation reaching the surface under perfectly clear sky (when sunshine duration equals the maximum $n = N$), that is b captures the incremental effect of increased sunshine duration (clearer skies) on total received radiation. To ensure their physical meaningfulness, the two parameters must meet the following numerical criteria:

- Non-negativity: $a > 0$ and $b > 0$. This ensures both parameters represent meaningful, physically realistic fractions, since negative values would imply a physically impossible scenario: negative radiation reaching the Earth's surface.
- Upper bound constraint: $a + b \leq 1$. This ensures the total fraction of extraterrestrial radiation reaching the Earth's surface on a perfectly clear day cannot exceed the radiation available at the top of the atmosphere.

Depending on atmospheric conditions (cloud types, humidity, dust) and solar declination (latitude and day of the year) the A–P coefficients may vary. Where no actual solar radiation data are available and no calibration has been carried out, common recommended values are $a = 0.25$ and $b = 0.50$.

If we define $R^* = \frac{H}{H_0}$ as the relative solar radiation (normalised H), and $n^* = n/N$ as the relative sunshine duration (normalised n). Rearranging Eq. (1), we get:

$$R^* = a + b\,n^* \tag{2}$$

where the coefficients a and b can be obtained by linear regression.

To achieve this, simultaneous data on sunshine duration (n) and shortwave radiation (H) are required. We can calculate H_0 and N

based on astronomical calculations given latitude and day of the year, allowing us to compute time series of R^* and n^*.

Following the FAO56 document [11], H_0 can be computed using the following sequence of equations:

Relative distance between Earth and Sun.

$$d_r = 1 + 0.033 \cos\left(\frac{2\pi J}{365}\right) \tag{3}$$

where J is the Julian day of the year (1 to 365).

Solar declination.

$$\delta = 0.409 \sin\left(\frac{2\pi J}{365} - 1.39\right) \tag{4}$$

Sunset hour angle.

$$\omega_s = \arccos\left(-\tan(\phi)\cdot\tan(\delta)\right) \tag{5}$$

where ϕ is the latitude in radians.

Extraterrestrial radiation.

$$H_0 = \frac{24\cdot 60}{\pi}\cdot G_{sc}\cdot d_r\cdot\left[\omega_s\cdot\sin(\phi)\cdot\sin(\delta)+\cos(\phi)\cdot\cos(\delta)\cdot\sin(\omega_s)\right] \tag{6}$$

where:

- H_0: Extraterrestrial radiation (MJ m^{-2} d^{-1})
- G_{sc}: Solar constant, equal to 0.082 MJ m^{-2} min^{-1}
- d_r: Relative Earth–Sun distance (dimensionless)
- δ: Solar declination (radians)
- ω_s: Sunset hour angle (radians)
- ϕ: Latitude (radians)

The maximum possible sunshine duration, or daylight hours N, can be computed from the sunset hour angle, ω_s:

Maximum possible sunshine duration.

$$N = \frac{24}{\pi}\cdot\omega_s \tag{7}$$

Following Eqs. (3)–(7), we can compute H_0 and N at each location and day for which we have observations of H and n, allowing to obtain time series of R^* and n^*.

2.3. Spatio-temporal model

The data represent observations from a spatio-temporal process $\{y(s,t),\ (s,t)\in D\subset\mathbb{R}^2\times\mathbb{R}\}$, measured at S spatial locations and T discrete time points. The spatio-temporal covariance function is defined as:

$$\mathrm{Cov}\left(y(\mathbf{s}_i,t), y(\mathbf{s}_j,u)\right) = C\left(y_{it}, y_{ju}\right) \tag{8}$$

Assuming spatial and temporal stationarity, the covariance function depends solely on the spatial distance $\Delta_{ij} = \| \mathbf{s}_i - \mathbf{s}_j \|$ and temporal lag $\Lambda_{tu} = | t - u |$, yielding:

$$\mathrm{Cov}(y_{it}, y_{ju}) = C(\Delta_{ij}, \Lambda_{tu}). \tag{9}$$

Under separability assumptions, this covariance can be decomposed into purely spatial and temporal covariance functions:

$$\mathrm{Cov}(y_{it}, y_{ju}) = C_1(\Delta_{ij})C_2(\Lambda_{tu}) \tag{10}$$

2.4. Hierarchical Bayesian spatio-temporal model

Let y_{it} denote the relative solar radiation R^* at spatial location $\mathbf{s}_i$, with $i = 1, \ldots, S$ and date $t = 1, \ldots, T$. We assume a Gaussian likelihood for the observations:

$$y_{it} \sim \mathcal{N}\left(\mu_{it}, \sigma^2\right) \tag{11}$$

where σ^2 represents the residual variance, assumed independent in space and time.

The linear predictor takes the form:

$$\mu_{it} = \alpha_{it} + \beta_{it}\cdot x_{it} \tag{12}$$

where x_{it} represents relative sunshine duration n^* at location i and time t, and α_{it} and β_{it} are spatio-temporal regression coefficients.

These coefficients are modelled as the sum of fixed effects (a_0 for α, and b_0, b_1 for β, respectively), latent spatio-temporal processes (ω_{it}, ϕ_{it}), and random effects accounting for site-level (ϵ_i, γ_i) and temporal variability (η_t, ι_t):

$$\alpha_{it} = \alpha_0 + \omega_{im(t)} + \epsilon_{im(t)} + \eta_t,\quad \beta_{it} = \beta_0 + \beta_1\,\mathrm{alt}_i + \phi_{im(t)} + \gamma_{im(t)} + \iota_t, \tag{13}$$

where alt_i represents the altitude at site i, and $m(t)$, $m = 1, \ldots, M$, represent the seasonal knot corresponding to time t (for instance, $M = 12$ can be used for a monthly seasonality).

The latent processes $\omega_{im(t)}$ and $\phi_{im(t)}$ capture seasonal spatio-temporal variability. They follow first-order autoregressive (AR(1)) temporal dynamics with spatially correlated innovations:

$$\omega_{im(t)} = \rho_\omega\,\omega_{im(t-1)} + \xi_{im(t)},\quad \phi_{im(t)} = \rho_\phi\,\phi_{im(t-1)} + \nu_{im(t)} \tag{14}$$

with circular and sum-to-zero constraints:

$$\begin{aligned}&\omega_{i1} = \rho_\omega\omega_{iM} + \xi_{i1},\ \ \phi_{i1} = \rho_\phi\phi_{iM} + \nu_{i1};\\ &\sum_{t=1}^{M}\omega_{im(t)=0},\ \ \sum_{t=1}^{M}\phi im(t) = 0.\end{aligned} \tag{15}$$

Here $\xi_{im(t)}$ and $\nu_{im(t)}$ are Gaussian fields, independent in time, defined by:

$$\mathrm{Cov}(\xi_{im(t)}, \xi_{ju}) = \begin{cases} 0 & \text{if } t \neq u \\ \mathrm{Cov}(\xi_i, \xi_j) & \text{if } t = u \end{cases} \tag{16}$$

for $i \neq j$, where $\mathrm{Cov}(\xi_i, \xi_j)$ is given by the Matérn spatial covariance function. An identical structure holds for ν_{im_t}. We denote the range and standard deviation of the Matérn field associated with the intercept a as ρ_ξ and σ_ξ, and those associated with the slope b as ρ_ν and σ_ν, respectively. ρ_ξ (ρ_ν), or range, controls the spatial correlation range — the distance beyond which spatial correlation becomes negligible. σ_ξ (σ_ν) determines the magnitude of spatial variability — the standard deviation of the underlying spatial field at a given location.

The site-specific random effects ϵ_{im} and γ_{im} account for station-level heterogeneity and seasonal variations, modelled as:

$$\epsilon_{im} \sim \mathcal{N}(0, \sigma_\epsilon^2),\quad \gamma_{im} \sim \mathcal{N}(0, \sigma_\gamma^2), \tag{17}$$

independent in space.

The temporal random effects η_{im} and ι_{im} account for temporal heterogeneity:

$$\eta_t \sim \mathcal{N}(0, \sigma_\eta^2),\quad \iota_t \sim \mathcal{N}(0, \sigma_\iota^2), \tag{18}$$

independent in time.

All components of the hierarchical Bayesian spatio-temporal model described above are summarised in the directed acyclic graph (DAG) presented in Fig. 3. The DAG highlights the hierarchical structure of the model, including observed data, covariates, latent effects, and hyperparameters, as well as their conditional dependencies. It provides a compact and transparent representation of how information flows across spatial and temporal levels in the model.

2.5. Priors

Semi-informative priors (Fig. 4) were defined as follows.

Fixed effects (α_0, β_0, β_1) were assigned Gaussian priors with mean 0.25 and precision 1/0.15. This choice reflects informative yet moderately diffuse prior beliefs based on both theoretical constraints and prior empirical knowledge. The intercept (α_0) and slope (β_0) coefficients of the A–P model are known to lie within the interval $[0, 1]$, since they

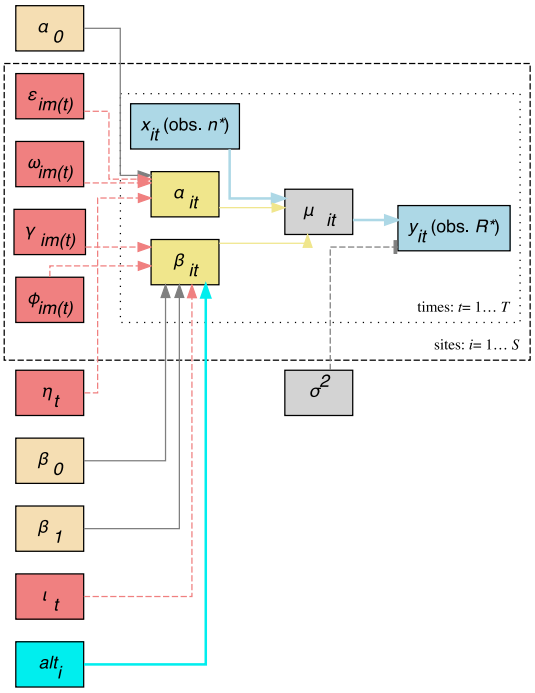

Fig. 3. Plate diagram of the hierarchical Bayesian spatio-temporal model. The outer dashed plate indexes spatial locations $i = 1, \ldots, S$, and the inner dotted plate indexes times $t = 1, \ldots, T$. Observed data (relative sunshine duration n^*_{it} and relative solar radiation R^*_{it}) are shaded light blue; the static covariate altitude alt_i is shaded cyan. Global fixed effects $(\alpha_0, \beta_0, \beta_1)$ are shaded wheat, and per-unit regression coefficients α_{it}, β_{it} are shaded khaki. Latent and random-effect components $(\omega_{im(t)}, \phi_{im(t)}, \epsilon_{im(t)}, \gamma_{im(t)}, \eta_t, \iota_i)$ are shaded light coral, while the deterministic linear predictor μ_{it} is shaded light grey. Solid coloured arrows denote deterministic or data flows (blue for observations, grey for fixed effects, azure for covariates, khaki for coefficient aggregation), and dashed coral arrows indicate stochastic contributions from latent and random effects.

represent fractions of extraterrestrial radiation transmitted under overcast and clear-sky conditions, respectively. Moreover, negative values are physically implausible, as surface radiation cannot be negative. The prior mean of 0.25 aligns with widely accepted baseline values recommended in the literature and operational guidelines—such as the Food and Agriculture Organisation of the Unitated Nations FAO-56 method for estimating reference evapotranspiration, which advises using $a = 0.25$ and $b = 0.50$ in the absence of local calibration [11]. These values are representative of typical atmospheric transmissivity under general conditions.

The prior on β_1, representing the effect of elevation on the slope coefficient, is similarly centred at 0.25. This reflects the expectation — based on the physics of radiative transfer — that higher-elevation sites, with thinner and less optically dense atmospheres, experience a stronger relationship between sunshine duration and surface radiation. Because elevation was standardised prior to model fitting, the magnitude of β_1 is expected to lie within a reasonable range around zero, and positive values are a priori more likely than negative ones. The Gaussian prior thus encodes prior information while remaining sufficiently flexible to accommodate empirical deviations.

Site-level and time-level random effects $(\sigma^2_\epsilon, \sigma^2_\gamma, \sigma^2_\eta, \sigma^2_\iota)$ were assigned penalized complexity (PC) priors, denoted $\text{PC}(\sigma; u, \alpha)$, with parameters $(u = 3, \alpha = 0.01)$. This formulation implies a weakly informative prior where the probability of the standard deviation exceeding u is $\text{P}(\sigma > u) = \alpha$. In our case, $\text{P}(\sigma > 3) = 0.01$, meaning that large and implausible levels of unexplained variability are penalised unless strongly supported by the data. The PC prior shrinks toward a simpler base model (i.e., no additional variability) but allows flexibility when there is empirical evidence for heterogeneity. This regularising behaviour is particularly useful in high-dimensional hierarchical models where overfitting is a concern [31].

For the autoregressive spatio-temporal components (ω, ϕ), we applied PC priors to the temporal correlation parameters ρ_ω and ρ_ϕ, using the form $\text{PC}(\rho; \rho_0, \alpha)$, where $\rho_0 = 0$ represents the base model (no autocorrelation). Specifically, we set $\text{P}(\rho > 0.9) = 0.01$, implying that strong temporal persistence is only accepted if clearly supported by the data. This approach avoids overly persistent dynamics by default, while still permitting them if necessary to capture seasonal structure. These PC priors strike a balance between regularisation and flexibility, ensuring stable inference in the presence of latent spatio-temporal components.

Finally, the Stochastic Partial Differential Equation (SPDE) model incorporated PC priors for the spatial range and marginal standard deviation of the latent fields. Specifically, we set $\text{P}(\text{range} < 10{,}000) = 0.01$ and $\text{P}(\sigma > 1) = 0.1$, thereby promoting smooth spatial transitions over medium to large distances while allowing for moderate spatial variability when supported by the data. These priors discourage overly short-range dependence and excessively rough spatial fields, aligning with the expected scale of atmospheric variability across the study domain.

2.6. Model fit

To fit this complex hierarchical Bayesian spatio-temporal model, we employed the Integrated Nested Laplace Approximation (INLA) method, as implemented in the R-INLA package [32,33]. INLA provides a computationally efficient alternative to traditional Markov Chain Monte Carlo (MCMC) methods by approximating posterior distributions numerically, significantly reducing computational cost. This approach utilises the SPDE approach for modelling spatial fields, enabling the inclusion of multiple hierarchical and latent structures, complex spatio-temporal interactions, and efficient exploration of posterior distributions. The use of INLA, particularly combined with the SPDE approach, is highly advantageous for large spatio-temporal datasets, providing accurate posterior estimates and predictive intervals while avoiding the computational demands typically associated with MCMC algorithms

3. Results

3.1. Exploratory analysis

Panel (a) of Fig. 5 presents histograms of the two main variables used in the analysis: relative solar radiation (R^*) and relative sunshine duration (n^*). Although both are dimensionless ratios bounded between 0 and 1, and their distributions appear similarly right-skewed, they exhibit important differences worth highlighting. The distribution of R^* peaks around 0.7, with few values exceeding 0.8 and virtually none reaching 1. This is physically consistent with the expectation that the amount of solar radiation reaching the Earth's surface is always attenuated by the atmosphere, due to absorption, scattering by gases and aerosols, and the presence of clouds. Even under the clearest conditions, some degree of atmospheric interference prevents full transmission of extraterrestrial radiation, hence values of R^* rarely — if ever — approach unity. In contrast, the distribution of n^* peaks closer to 0.85 and exhibits a substantial number of observations at or near 1, indicating that many days experience sunshine duration equal to the maximum possible daylight length—typical of cloud-free days. The difference between the two distributions is especially evident in their lower tails. While R^* gradually tapers off toward zero, with relatively few days showing extremely low values, the distribution of n^* shows clear zero-inflation: a pronounced concentration of values at or very near zero. This discontinuity is due to the way sunshine duration is measured, using threshold-based instruments that do not register sunshine unless a minimum direct irradiance level is exceeded. Consequently, overcast days, during which this threshold is rarely reached, are often recorded

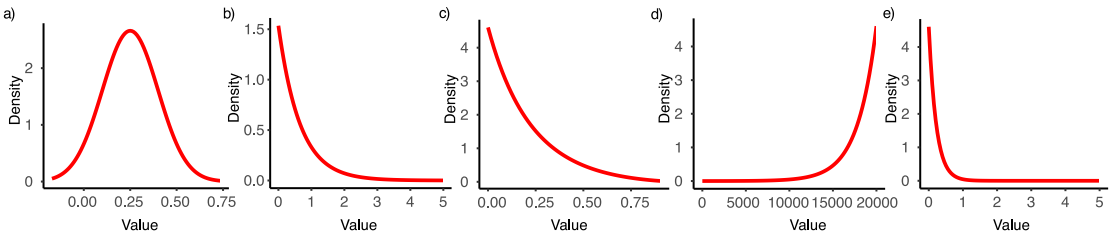

Fig. 4. Prior distributions of the model parameters: (a) fixed effects ($\alpha_0, \beta_0, \beta_1$); (b) site-level and time-level random effects ($\sigma_\epsilon^2, \sigma_\gamma^2$); (c) auto-regressive spatial fields (ρ_ω, ρ_ϕ), (d) SPDE range; (e) SPDE standard deviation.

as having zero sunshine duration. This artefact of the measurement method may have implications for modelling and should be taken into account when interpreting or fitting statistical models to these data.

Panel (b) of Fig. 5 displays a two-dimensional histogram (heat map) showing the joint distribution of relative solar radiation (R^*) and relative sunshine duration (n^*), along with a loess-smoothed curve that summarises the relationship between both variables. The overall pattern supports the empirical relationship proposed by the Angström–Prescott model, with a clear and nearly linear association across most of the observed range. This indicates that sunshine duration is indeed a good predictor of solar radiation, reinforcing the potential of the A–P model to explain the variability in R^*. However, the lower part of the distribution reveals a noticeable deviation from linearity: for values of R^* below approximately 0.25, the corresponding n^* values tend to concentrate around zero, offering little explanatory power. This anomaly stems from the threshold-based nature of sunshine duration measurements, as discussed earlier. Because values of n^* are often recorded as zero during overcast days — when radiation levels are low but non-zero — the lower end of the distribution of n^* becomes saturated with zeros, failing to capture the finer variability in actual solar radiation. As a result, the predictive accuracy of n^* in the low-radiation regime is diminished, introducing a systematic limitation that should be accounted for in model development and interpretation.

Another apparent effect is that, while the overall relationship between the two variables appears linear, the loess curve flattens slightly at the upper end—especially when n^* approaches 1. This suggests a saturation effect where additional sunshine duration contributes less proportionally to surface radiation. This may reflect the influence of high sun angles, diffuse radiation, or a ceiling imposed by other atmospheric factors like aerosols or humidity, which limit how much radiation actually reaches the surface even on clear-sky days.

It is important to note that the exploratory analyses presented in Fig. 5 aggregate all available data without accounting for potential seasonal effects. Seasonal variability in atmospheric conditions, solar angle, and cloud patterns may influence the distributions and relationships observed, and will be explicitly addressed in the modelling framework.

3.2. Spatio-temporal model: fixed and latent components

Figs. 6 and 7 present the posterior estimates of the fixed effects in the Angström–Prescott model. Fig. 6 shows the marginal posterior distributions of the intercept (α_0), the baseline slope coefficient (β_0), and the altitude-dependent effect on the slope (β_1). All three coefficients are well-identified, with their 95% credible intervals excluding zero, indicating strong evidence of a systematic relationship. The median posterior estimates are $\alpha_0 = 0.120$ [0.107, 0.132], $\beta_0 = 0.387$ [0.347, 0.428], and $\beta_1 = 0.041$ [0.016, 0.066]. These results suggest that both the intercept and slope of the A–P model vary consistently across the dataset, and that altitude plays a positive and significant role in modulating the slope coefficient (b).

Fig. 7 maps the combined effect $\beta_0 + \beta_1 \cdot \text{alt}_i$, reflecting the spatial structure of the slope coefficient b across the study area. Higher values of the slope are observed in elevated regions, such as mountain ranges (Pyrenees, Cantabrian and Iberian Ranges, Central and Betic Systems) or the Northern Plateau, which may be explained by thinner atmospheres at higher altitudes allowing more direct radiation per unit of sunshine duration. Other candidate geographical predictors such as latitude or distance to the sea were tested but excluded from the final model, as their posterior credible intervals included zero. Similarly, no consistent spatial pattern was detected for the intercept term (a), and no geographic covariates were retained for this component.

Fig. 8 displays the posterior marginal distributions of key hyperparameters in the model, including the overall observation error (σ), the parameters of the latent spatial fields for the intercept (a) and slope (b), as well as the standard deviations of the unstructured temporal and site-level random effects. Red points indicate posterior medians, and red lines denote 95% credible intervals. Below we discuss each parameter in turn.

Observation error (σ): The posterior median of the residual standard deviation is low, indicating that the hierarchical model captures much of the variability in R^*, with only limited unexplained noise. This supports the adequacy of the model structure and the inclusion of relevant covariates and latent components.

Latent spatial field for a (intercept):

- *Range* (ρ_ξ): Posterior density suggests a moderate-to-large spatial range, implying that spatial correlation in the intercept component extends over wide distances.
- *Standard deviation* (σ_ξ): This value is relatively small compared to the slope field, indicating limited spatial variability in the intercept.
- *Autocorrelation* (ρ_ω): High posterior mass near 1 suggests strong temporal dependence in the latent intercept process, reinforcing the seasonal structure captured by the model.

Latent spatial field for b (slope):

- *Range* (ρ_ν): Similar to ρ_ξ, the spatial field for the slope also exhibits long-range dependence, suggesting smooth geographical transitions in the sensitivity of R^* to n^*.
- *Standard deviation* (σ_ν): This is markedly larger than σ_ξ, indicating that the slope coefficient (b) varies more substantially in space than the intercept.
- *Autocorrelation* (ρ_ϕ): Also concentrated near 1, reflecting strong temporal persistence in the slope field, consistent with a smoothly evolving seasonal process.

Unstructured temporal effects:

- *Standard deviation for a* (σ_η): Posterior density indicates modest temporal variability in the intercept not explained by the structured latent field.
- *Standard deviation for b* (σ_ι): Larger than σ_η, implying more pronounced unstructured temporal variation in the slope, possibly due to transient meteorological or instrumental factors.

Unstructured site-level effects:

- *Standard deviation for a* (σ_ϵ): Relatively small, suggesting limited local variability in the intercept across stations.

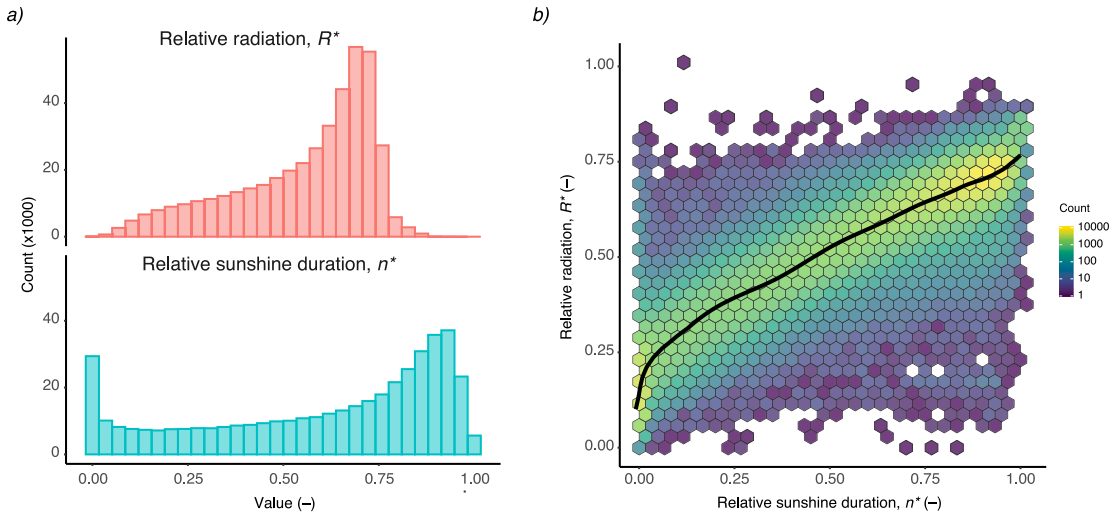

Fig. 5. Exploratory analysis of the two main variables in the study: (a) histograms of relative solar radiation (R^*, top) and relative sunshine duration (n^*, bottom); (b) joint distribution of R^* and n^* shown as a two-dimensional histogram (heat map), with a loess-smoothed curve overlaid.

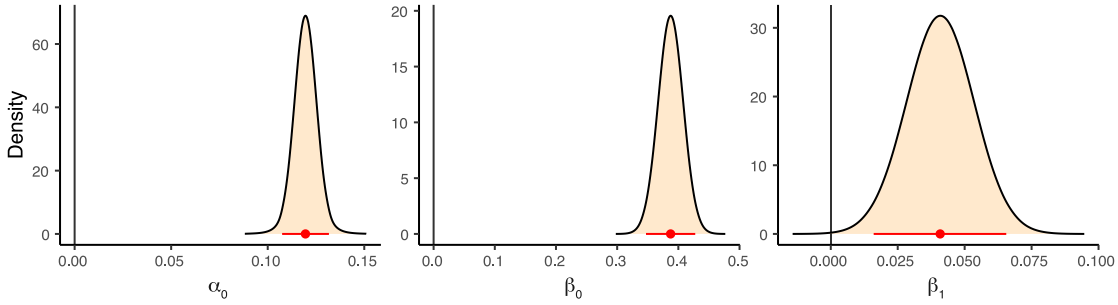

Fig. 6. Posterior marginal distributions of the fixed effects in the Angström–Prescott model: α_0 (intercept), β_0 (baseline slope), and β_1 (altitude effect on the slope). Red dots denote the posterior medians, and red lines represent the 95% credible intervals.

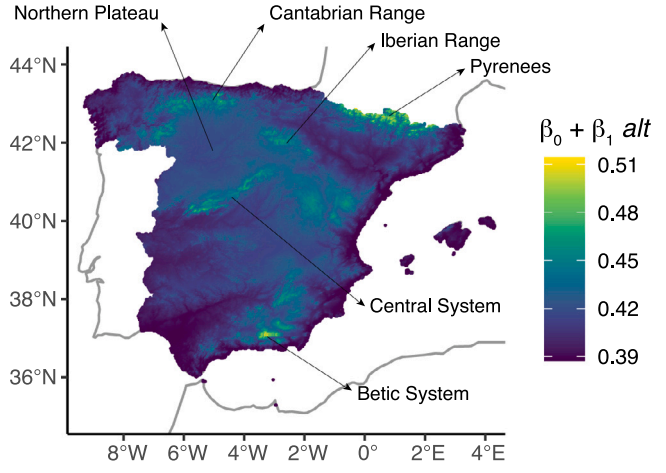

Fig. 7. Spatial distribution of the slope coefficient b in the Angstrom–Prescott model, computed as the linear combination $\beta_0 + \beta_1 \cdot \text{alt}_i$.

- *Standard deviation for* b (σ_γ): Notably larger, consistent with the spatial field analysis, and reinforcing that the slope term b is more sensitive to location-specific characteristics than the intercept a.

Taken together, these results indicate that spatial and temporal heterogeneity is more pronounced in the slope coefficient (b) than in the intercept (a), reflecting a stronger geographical modulation of the sensitivity of radiation to sunshine duration.

Figs. 9 and 10 display the monthly spatial fields for the latent spatio-temporal effects ω (intercept) and ϕ (slope) of the Angström–Prescott model, respectively. Each figure contains 12 panels, corresponding to each month of the year. Thanks to the autoregressive temporal structure, the fields evolve smoothly throughout the seasons, exhibiting coherent spatial gradients typically oriented along NW–SE or N–S axes. These patterns suggest systematic regional differences in the local radiative climate and its seasonal modulation. The fields for ϕ show larger spatial contrasts and greater overall magnitude than those for ω, indicating a more pronounced and spatially heterogeneous seasonal modulation in the slope coefficient b (i.e., the sensitivity of R^* to n^*) than in the intercept a.

Seasonal averages of the spatial effects, shown in Fig. 11, reveal an interesting temporal contrast. The mean value of ω follows a distinct unimodal pattern, reaching a minimum in winter (December–January) and peaking in summer (July). This is consistent with increased baseline levels of relative radiation during the sunniest part of the year, independent of sunshine duration. Conversely, ϕ exhibits an inverted seasonal cycle, with a maximum in February and a minimum in July, along with a secondary maximum in October. This implies that the explanatory power of sunshine duration — i.e., the slope of the A–P relationship — is strongest in late winter and weakest in midsummer.

The spatial fields ω and ϕ shown in Figs. 9 and 10 exhibit notable latitudinal gradients, particularly pronounced during summer months. The intercept-related field (ω) consistently shows a clear north–south gradient, with higher values toward the southern regions and lower values to the north. This indicates that, independent of sunshine duration, southern locations receive relatively higher fractions of extraterrestrial radiation. Such a pattern is physically plausible, as southern regions

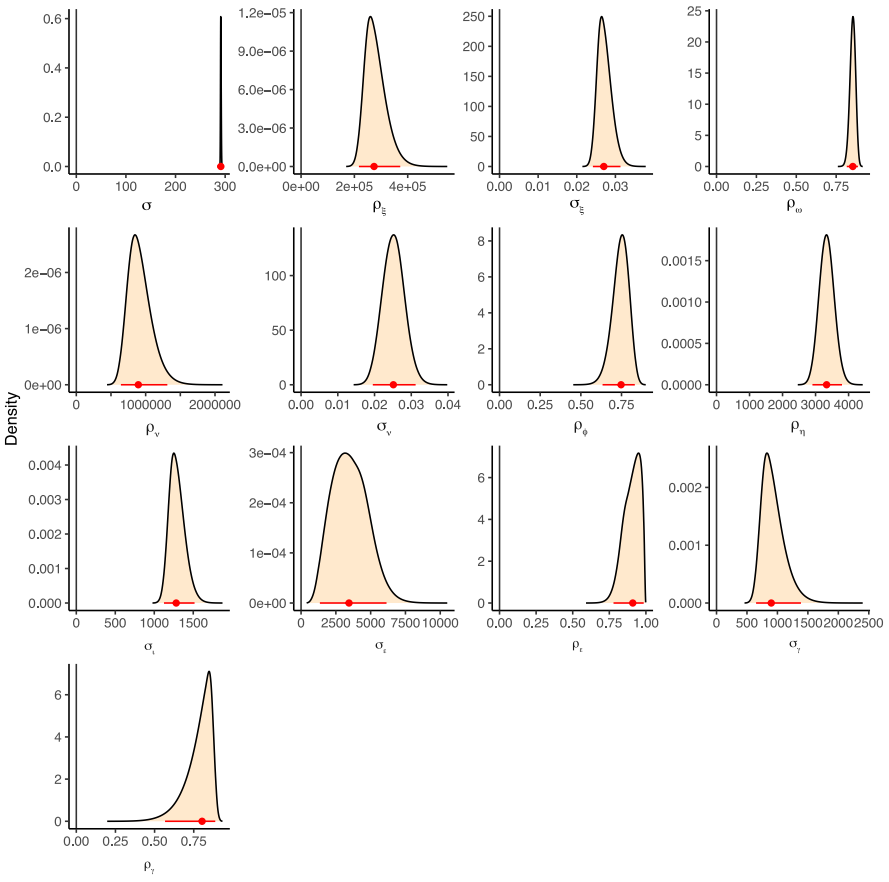

Fig. 8. Posterior marginal distributions of the fixed effects in the Angström–Prescott model: overall standard deviation (σ); range (ρ_ξ), standard deviation (σ_ξ) and autocorrelation (ρ_ω) of the a spatio-temporal field; range (ρ_ν), standard deviation (σ_ν) and autocorrelation (ρ_ϕ) of the b spatio-temporal field; standard deviation of the random temporal effects for α (σ_η) and β (σ_ι); and standard deviation of the random spatial effects for a (σ_ϵ) and b (σ_γ). Red dots denote the posterior medians, and red lines represent the 95% credible intervals.

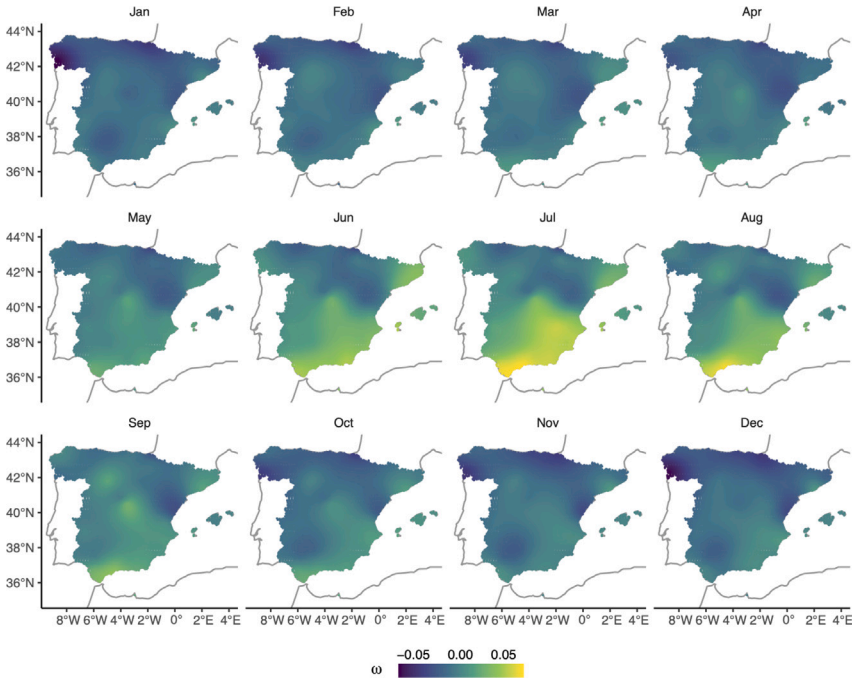

Fig. 9. Monthly spatial fields of the latent spatio-temporal component ω, associated with the intercept (a) of the Angström–Prescott model. Each panel corresponds to a calendar month.

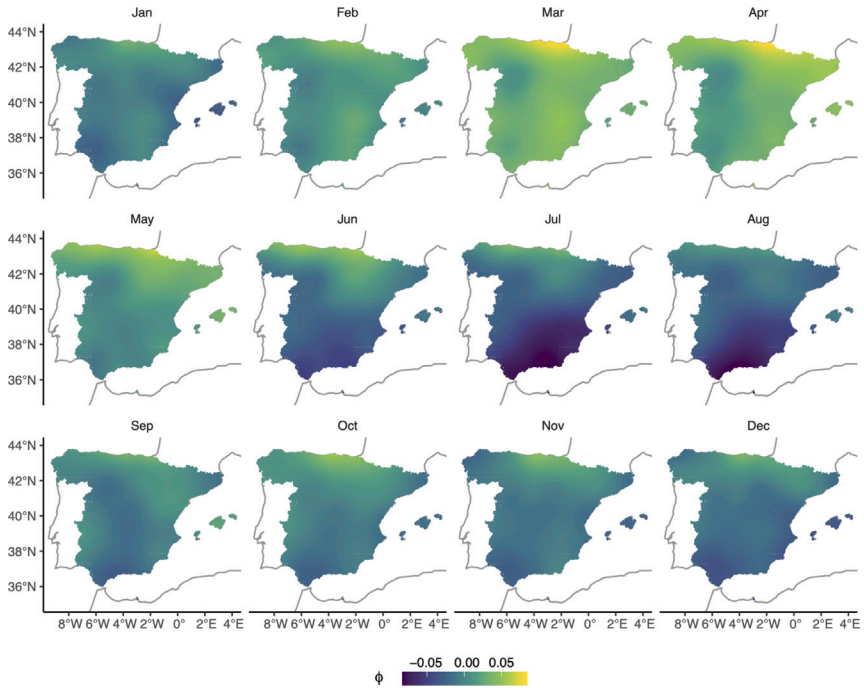

Fig. 10. Monthly spatial fields of the latent spatio-temporal component ϕ, associated with the slope (b) of the Angström–Prescott model.

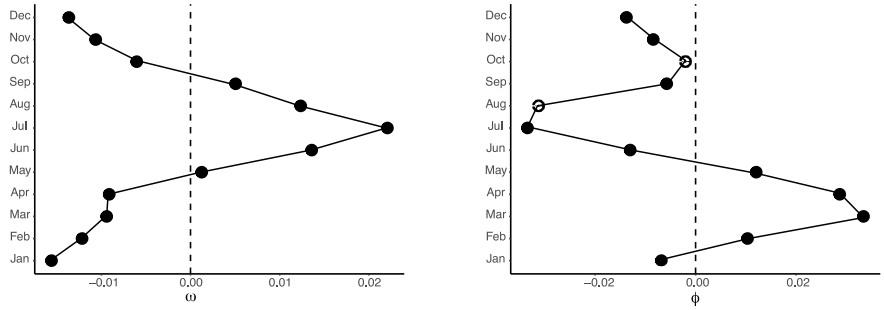

Fig. 11. Monthly means of the spatial fields ω (left) and ϕ (right), summarising the seasonal evolution of the intercept and slope components of the Angström–Prescott model.

are typically characterised by clearer skies and lower cloud coverage, especially pronounced in the summer.

Conversely, the slope-related field (ϕ) presents an opposite gradient during summer, with lower values in the south and higher values in the north. This suggests that, despite southern regions receiving higher baseline radiation, the incremental contribution of increased sunshine duration to surface radiation diminishes. This phenomenon can be explained by increased atmospheric turbidity during summer months in southern areas, possibly due to higher aerosol loading, dust intrusion, or enhanced atmospheric scattering [34]. In northern regions, where clearer air conditions prevail during sunny periods, additional sunshine duration translates more efficiently into increased radiation, thus elevating the slope (b) of the Angström–Prescott model. During winter, typically characterised by frequent cloud cover and higher humidity, the spatial gradients weaken, indicating a more homogeneous radiative environment across the study area. These complementary spatial patterns reinforce the physical interpretations of the intercept and slope parameters and highlight the influence of regional climatological and atmospheric conditions on the solar radiation regime.

Fig. 12 shows the full posterior densities of the two model parameters, reflecting how the model's combination of fixed effects and spatio-temporal latent fields causes a to vary around its central value. The FAO-56 values are marked by dots at the bottom of the plots, revealing that the model's a distribution spans both above and below

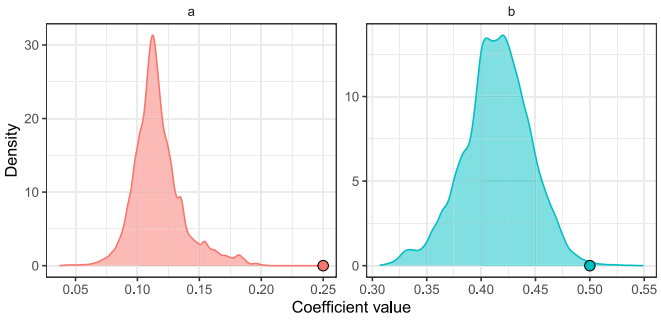

Fig. 12. Posterior kernel density estimates of the Angström–Prescott intercept (a, left panel) and slope (b, right panel) coefficients, integrating the fixed and latent spatio-temporal effects across all stations and seasons. Coloured dots at the bottom of each panel indicate the standard FAO-56 coefficients (a = 0.25; b = 0.50), for reference.

that standard constant. In both panels, the width and shape of each density illustrate the extent of spatial and seasonal variability: rather than collapsing a and b to single fixed numbers, our model allows these coefficients to adapt to local conditions, while the FAO-56 values remain valid but do not capture that full range of variation.

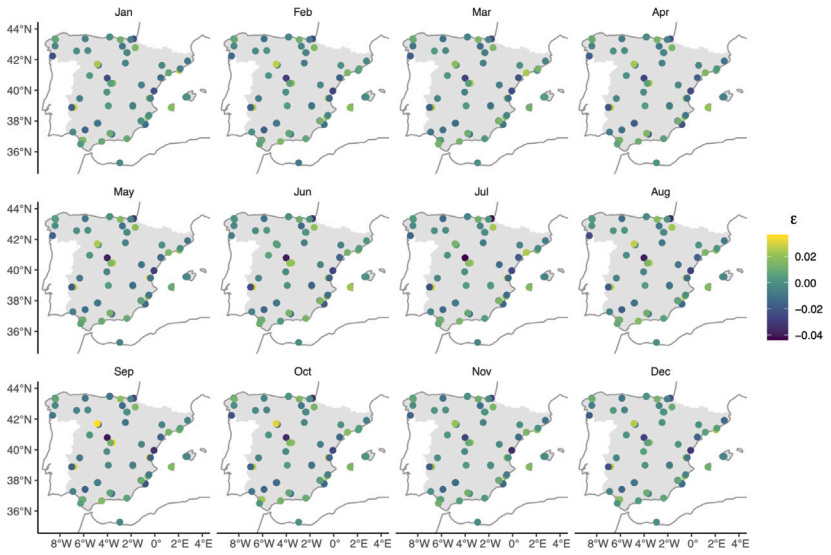

Fig. 13. Monthly spatial fields of the site-specific random effect ϵ, associated with the intercept (a) of the Angström–Prescott model.

3.3. Random components

Figs. 13 and 14 show the monthly spatial fields of the random site-specific effects ϵ and γ, which represent deviations in the intercept (a) and slope (b) of the Angström–Prescott model, respectively. These fields capture spatially unstructured heterogeneity across measurement stations. The patterns reveal that most of the variation occurs across sites rather than across months, with each station tending to maintain consistent deviations over time. This stability suggests that certain stations systematically record higher or lower radiation levels (R^*) or exhibit different sensitivity to sunshine duration (n^*), even after accounting for covariates and structured spatio-temporal effects.

The magnitude of these site-specific effects is moderate but non-negligible. For ϵ, deviations typically range between −0.04 and +0.02, while for γ they extend from approximately −0.08 to +0.04, as indicated by the colour scales. These patterns are consistent with the posterior distributions of the corresponding hyperparameters (Fig. 8), which show posterior medians of σ_ϵ and σ_γ around 0.01–0.02, the presence of weak unexplained spatial heterogeneity. The larger spread observed for γ compared to ϵ reinforces previous findings that the slope coefficient (b) is more spatially variable than the intercept (a), likely due to its greater sensitivity to local atmospheric or observational conditions.

These site-specific discrepancies may reflect localised characteristics not explicitly modelled, such as instrumentation differences, calibration biases, shading or horizon obstruction, persistent cloud microclimates, or undocumented land use conditions. The presence of non-negligible and stationary site effects supports the inclusion of these random terms in the model to absorb local idiosyncrasies and improve the generalisation of the estimated spatial fields.

Fig. 15 presents the temporal evolution of the monthly random effects η and ι, which represent unstructured temporal variability in the intercept (a) and slope (b) components of the Angström–Prescott model, respectively. These effects are grouped into 607 monthly blocks spanning the period from 1973 to 2020. This temporal aggregation was necessary due to computational constraints arising from the large size of the dataset (over 18,000 daily records), and we acknowledge that this constitutes a simplification of the underlying daily variability.

Despite this simplification, several relevant patterns emerge. First, the magnitudes of η and ι are comparable to those of the site-specific effects discussed earlier. The posterior distribution of their standard deviations (Fig. 8) indicated values around 0.01–0.02, consistent with the vertical spread observed in the time series. However, ι exhibits higher temporal variability than η, indicating that the slope (b) of the model is more sensitive to changes over time than the intercept (a). This asymmetry is consistent with previous findings from the spatial and spatio-temporal components, where variability in b was generally greater than in a.

Most notably, the time series of ι displays a visible long-term shift, particularly Ignoring the first two years (1973–1975), where data coverage is sparse, we observe a gradual increase in ι, peaking around 2010, followed by a slight downward trend thereafter. This suggests a possible long-term trend in the sensitivity of solar radiation to sunshine duration in our study region, potentially driven by changes in atmospheric transmissivity—such as reductions in air pollution, variations in aerosol loading, or shifts in cloud dynamics.

In contrast, the η component remains relatively stable, fluctuating around zero with no evident long-term trend. This stability indicates that the baseline level of relative radiation (intercept) is less affected by temporal drivers, and that most of the temporal modulation in the radiation–sunshine relationship occurs through changes in the slope parameter.

3.4. Model validation

Fig. 16 provides validation statistics for our hierarchical Bayesian model (M1) and for an alternative model with fixed FAO-56 coefficients (M0). Looking first at the mean absolute error (MAE), assessing deviations between predicted and observed values, M1 consistently yields smaller errors than M0 in every month. Both monthly and annual-average statistics show that replacing the FAO-56 fixed coefficients with spatially and seasonally varying, elevation-informed parameters (M1) substantially reduces error, eliminates seasonal bias, better preserves the natural spread of observed radiation, and boosts explained variance.

For example, while M0's MAE declines from 0.057 in January to about 0.040 in July before rising back to 0.06 in December, M1's MAE starts at 0.048 in January, dips to 0.033 in July, and ends near 0.05 in December. On an annual basis, this corresponds to a reduction from MAE = 0.0491 (M0) to MAE = 0.042 (M1). The mean error (ME), a bias indicator, shows that M1 maintains virtually zero bias all year. By contrast, M0 exhibits positive bias in winter (up to +0.02 in January and +0.025 in December) and negative bias in spring (around –0.014 in April–May). Turning to variance reproduction (ratio of standard deviations, RSD), an RSD of 1 would mean the model's spread exactly matches that of the observations. M1's RSD hovers between 0.94 and 0.95 across all months, demonstrating only slight under-dispersion.

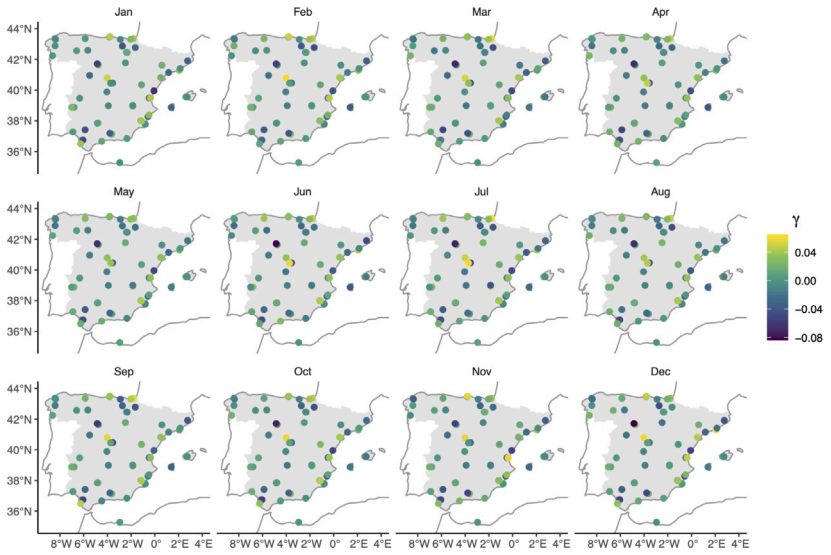

Fig. 14. Monthly spatial fields of the site-specific random effect γ, associated with the slope (b) of the Angström–Prescott model.

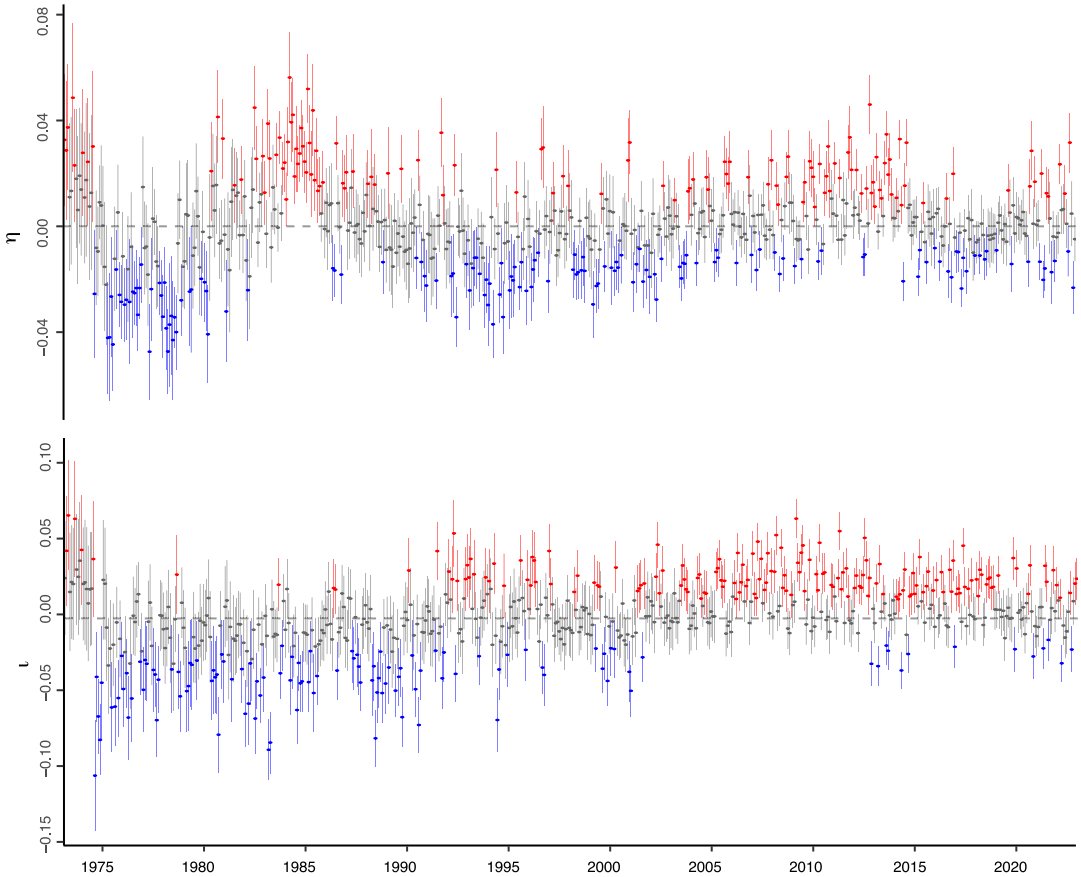

Fig. 15. Temporal evolution of the monthly random effects η (top) and ι (bottom), representing unstructured temporal variability in the intercept (a) and slope (b) components of the Angström–Prescott model, respectively.

M0, however, varies from 0.831 in March to 0.90 in July, meaning it systematically underestimates variability, particularly in spring. Over the entire year, M0 achieves RSD = 0.869, whereas M1 improves this to RSD = 0.947. Finally, the coefficient of determination (R^2) confirms that M1 captures more of the observed variance than M0 in every month. In winter and early spring (January through April), M1's R^2 climbs up to 0.91 (March), while M0 peaks at around 0.87. Although both models experience a dip in midsummer (June–July), M1 remains near 0.87–0.88, while M0 falls to 0.82–0.83. Annually, M0's overall R^2 is 0.870 compared to 0.899 for M1.

Fig. 17 shows a comparison between observed and model-predicted density distributions of relative solar radiation (R^*), disaggregated by month. Overall, the model performs well in replicating the empirical distribution, particularly for medium to high values of R^*. In most months, the predicted densities closely follow the observed ones in the range $R^* > 0.5$, indicating that the model effectively captures the

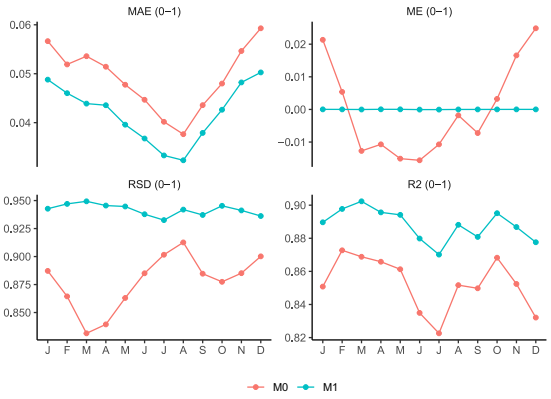

Fig. 16. Monthly validation statistics for the fixed-coefficient A–P model (M0) versus our hierarchical Bayesian model (M1): mean absolute error (MAE), mean error (ME), ratio of standard deviations (RSD), and coefficient of determination (R^2), plotted from January (J) through December (D). All values range between 0 and 1.

central tendency and variability of radiation under moderately clear to very clear sky conditions.

However, a systematic discrepancy emerges in the lower range of R^*, most conspicuous during the winter months when overcast days are more prevalent. For values below 0.5 — and especially below 0.35 — the predicted distributions tend to concentrate mass around $R^* \approx 0.25$, whereas the observed densities show a more progressive decline toward zero. Mean absolute error (MAE) computed by splitting the sample clearly reflects this situation, with an average value of 0.038 for observed $R^* > 0.35$, compared to 0.060 (almost double) for $R^* < 0.35$. Similarly, the mean error (ME) shifted from −0.009 (virtually unbiassed) for $R^* > 0.35$ to 0.040 for $R^* < 0.35$, indicating a tendency toward systematic over-estimation in the lower range of R^*.

This mismatch reflects a limitation in the model's ability to reproduce the lower tail of the radiation distribution, particularly during overcast conditions. As discussed in the exploratory analysis (Fig. 5), this phenomenon likely arises from how sunshine duration (n^*) is measured. The sunshine recorders only detect sunshine above a threshold irradiance level, causing all sub-threshold values to be recorded as zero. This results in a zero-inflated distribution for n^* at low values, leading to a loss of information about radiation variability under cloudy conditions. Consequently, the model struggles to distinguish between moderate and extremely low radiation values when $n^* \approx 0$, effectively collapsing these cases toward a central predicted value around $R^* \approx 0.25$.

Despite this limitation, the close match in the upper range validates the overall structure of the model and confirms its reliability in reproducing seasonal and distributional patterns of solar radiation under most sky conditions. The observed under-dispersion in the lower tail highlights the importance of measurement limitations in sunshine duration and motivates future efforts to improve modelling performance under fully overcast skies.

4. Discussion

4.1. Model performance and validation

Our hierarchical Bayesian implementation of the Angström–Prescott model demonstrated a strong ability to capture the main patterns and sources of variability in daily relative solar radiation (R^*) across Spain. Both the fixed effects and latent components contributed meaningfully to model accuracy, with statistically significant posterior distributions for all fixed parameters, including the intercept (α_0), slope (β_0), and the altitude-dependent effect on the slope (β_1).

In particular, the fitted distributions closely followed the observed ones, especially in the medium to high range of R^* (> 0.35), indicating that the model is able to accurately reproduce the typical and clear-sky radiation conditions. Deviations were primarily confined to the lower tail of the distribution, where the model tended to underrepresent the frequency of low radiation values. This pattern is consistent with the known limitations of sunshine duration data, particularly the instrument's threshold effect that results in a zero-inflated distribution of n^* under overcast conditions.

Despite these limitations, the overall agreement between observed and predicted densities across all months underscores the suitability of the A–P framework for estimating solar radiation from sunshine duration. The spatio-temporal extensions implemented here significantly enhance the traditional model's flexibility and accuracy, allowing for dynamic, location- and time-specific calibration of the empirical coefficients. This feature is particularly valuable in regions or time periods with limited direct radiation measurements, offering a statistically principled approach to inferring missing or incomplete solar radiation data.

4.2. Interpretation of spatial and seasonal variability

One of the key strengths of the hierarchical model structure lies in its ability to decompose spatial and seasonal patterns in the empirical coefficients of the Angström–Prescott equation. The spatially structured latent fields ω (intercept) and ϕ (slope), along with their seasonal evolution, reveal coherent and interpretable patterns across the Iberian Peninsula. These fields vary smoothly across space and time, reflecting the influence of underlying climatological and geographic factors on the radiation–sunshine relationship. Seasonal variation in both the intercept (a) and slope (b) coefficients has been previously highlighted as important for accurate radiation modelling [35]. Our results confirm this, while incorporating seasonally-varying spatial gradients in both coefficients.

The spatial fields of ω exhibit a persistent north–south gradient, with lower intercept values in the north and higher values in the south, particularly during summer. Since the intercept represents the baseline level of radiation when sunshine duration is zero, this pattern likely reflects regional differences in atmospheric clarity, cloud structure, and background diffuse radiation. Southern regions, which are generally drier and experience clearer atmospheric conditions, tend to register higher R^* values even under partially overcast skies, while northern areas are more frequently affected by persistent cloud cover.

The slope field ϕ, in contrast, displays an opposing north–south gradient during the summer months, with the slope of the A–P relationship being strongest in the north and weakest in the south. This indicates that additional sunshine duration in northern areas is more strongly associated with increases in surface radiation, possibly due to clearer air and lower atmospheric turbidity. In southern regions, where the atmosphere is often hazier and more laden with aerosols — especially during the summer months — additional sunshine does not translate as efficiently into increased surface radiation, leading to flatter slopes. These contrasting spatial gradients support the interpretation that the slope parameter (b) captures the radiative efficiency of sunshine, while the intercept (a) reflects baseline diffuse radiation levels.

The monthly averages of ω and ϕ spatial fields further highlight this complementarity. The intercept component ω peaks in July, following the seasonal maximum in solar elevation and radiation availability, while ϕ reaches a minimum during the same period. Conversely, ϕ shows a secondary maximum in late winter to early spring (February–March), when atmospheric variability is higher and the predictive value of sunshine duration is enhanced.

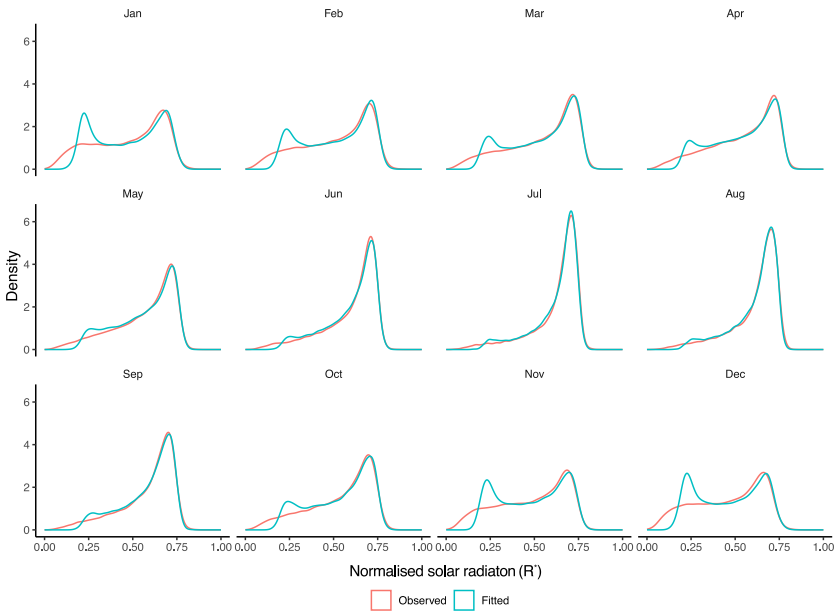

Fig. 17. Comparison between observed (red) and model-predicted (blue) monthly density distributions of relative solar radiation (R^*). Each panel corresponds to a different month.

4.3. Role of elevation

Among the geographic covariates considered, elevation emerged as the only one with a statistically significant and interpretable effect on the parameters of the Angström–Prescott model. The inclusion of an interaction term between elevation and sunshine duration improved model performance and revealed a clear positive effect of altitude on the slope coefficient (b). This suggests that at higher elevations, the relationship between sunshine duration and incoming solar radiation becomes stronger, meaning that an additional hour of sunshine corresponds to a greater increase in surface radiation, as suggested in earlier studies [36].

This pattern is consistent with known physical mechanisms. Higher-elevation sites typically experience reduced atmospheric path lengths and lower aerosol concentrations, resulting in increased direct beam radiation and less attenuation. The thinner atmosphere allows more of the extraterrestrial solar radiation to reach the surface during sunny periods, thereby amplifying the radiative gain per unit of sunshine duration.

In contrast, other candidate geographic variables, including latitude, longitude, and distance to the sea, were tested but ultimately excluded from the final model due to their lack of statistical significance. Their posterior credible intervals included zero, and their inclusion did not improve predictive performance. This result suggests that the structured spatio-temporal fields incorporated in the model already absorb the large-scale spatial variation typically associated with these covariates. In particular, the latent spatial fields for the intercept and slope effectively account for broad regional gradients, rendering additional fixed geographic terms redundant. The exclusion of latitude as a fixed effect also underscores the importance of modelling extraterrestrial radiation explicitly (via H_0), which already incorporates geographic and astronomical dependencies such as latitude and time of year.

4.4. Long-term temporal variability and trends

Beyond seasonal and spatial variation, our model reveals evidence of low-frequency temporal dynamics in the relationship between sunshine duration and surface radiation. The temporal random effects η and ι, representing unstructured variability in the intercept and slope components of the model, respectively, were aggregated into 607 monthly blocks over the study period. Despite this coarse temporal resolution, their time series reveal important insights into decadal trends.

The η component, associated with baseline radiation levels (a), remains relatively stable throughout the study period, fluctuating around zero with no systematic drift. This suggests that the overall background radiation levels — modulated primarily by seasonal astronomical factors and broad-scale atmospheric conditions — have remained stationary over the past five decades.

In contrast, the ι component, associated with the slope coefficient (b), exhibits more pronounced long-term variability. Excluding the early years of sparse data (1973–1977), we observe a progressive increase in ι reaching a peak in the early 1990s, followed by a gradual decline and partial recovery thereafter. Since the slope coefficient quantifies the sensitivity of surface radiation to sunshine duration, this trend may reflect evolving atmospheric transmissivity over time. An increase in ι implies that an additional hour of sunshine results in a greater amount of incoming radiation, which could signal a period of atmospheric clearing, potentially linked to reductions in aerosol emissions or improvements in air quality. The subsequent decline may point to increased atmospheric turbidity or changing cloud optical properties, although attribution requires caution since instrument calibration shifts (e.g., plate aging or maintenance schedules) could also produce similar changes in slope.

These results complement those of Sanchez-Lorenzo et al. [8], García et al. [37], Rom00E1n et al. [28], and Antón et al. [29], who identified periods of “global dimming” and “brightening” in Spain and attributed these to changing aerosol loads and cloud dynamics. However, the distinction between the trends of both components of the A–P equation has not been made explicit in previous studies and underscores the added value of our spatio-temporal modelling framework, which is capable of separating structured trends in radiation sensitivity from background levels and local noise. While previous efforts have focused primarily on empirical model calibration [30] or reconstruction of radiation records [28], our work offers a unified statistical treatment that integrates structured and unstructured seasonal, spatial, and temporal variability with explicit uncertainty quantification.

These long-term effects align also with documented environmental changes across Europe. The increase in slope sensitivity during the 1980s and early 1990s corresponds with the implementation of significant environmental regulations aimed at reducing industrial emissions and improving air quality. For instance, the European Union

introduced directives targeting sulfur dioxide and nitrogen oxide emissions during this period [38], leading to substantial decreases in these pollutants [39]. Such reductions likely enhanced atmospheric clarity, thereby increasing the efficiency of solar radiation transmission.

4.5. Limitations of sunshine duration data and implications for uncertainty

While sunshine duration is a valuable and widely available proxy for estimating surface solar radiation, its use has important limitations that affect model performance, particularly under overcast conditions. Traditional sunshine recorders, such as the Campbell–Stokes heliograph used in many long-term observational networks, only register sunshine when direct irradiance exceeds a predefined threshold [40]. As a result, all sub-threshold irradiance values — typical of overcast days — are recorded as zero, regardless of subtle variability in actual radiation levels Almorox et al. [35].

This hard threshold leads to a censoring effect in the sunshine duration record, especially in the low end of the radiation distribution. As a result, when $n^* \approx 0$, the model cannot reliably distinguish between moderately cloudy and fully overcast conditions, because all corresponding sunshine inputs are identically zero. In the validation analysis, this manifests as an over-concentration of predicted values around $R^* \approx 0.25$, with the model failing to reproduce the observed variability in lower radiation regimes ($R^* < 0.25$).

This systematic under-dispersion at low n^* is not merely a statistical artefact, as it has practical consequences for applications such as solar energy yield estimation. In regions or seasons with frequent overcast conditions, the inability to capture low radiation variability may lead to biased yield estimates, particularly for technologies sensitive to diffuse versus direct radiation components. For example, photovoltaic (PV) system design and performance simulations often rely on realistic representations of intra-daily and daily radiation variability; a flattened or biased distribution at the low end can result in overestimated reliability metrics, suboptimal sizing, or flawed economic assessments.

These limitations underscore the need for caution when applying sunshine-based radiation models to contexts where accurate estimation of low-radiation conditions is critical. Future work could address this by incorporating covariates more sensitive to low-light variability such as cloud fraction, satellite-derived albedo, or visibility, or by developing latent measurement error models that explicitly account for the censoring introduced by sunshine recorders. Accounting for systematic differences between instrument types, as discussed by Almorox et al. [35], may also improve generalisation in multi-source datasets.

4.6. Methodological strengths and broader implications

A key contribution of this study lies in its methodological framework. By embedding the empirical Angström–Prescott model within a hierarchical Bayesian spatio-temporal structure, we extend its applicability well beyond simple site-specific regression. The use of the Integrated Nested Laplace Approximation (INLA) framework, in combination with the SPDE approach, provides a computationally efficient and fully probabilistic means to estimate model parameters, quantify uncertainty, and accommodate complex spatial and temporal dependencies.

This modelling structure offers several advantages. First, it supports partial pooling of information across stations and time periods, thereby improving parameter estimation in locations with sparse or incomplete data. Second, the model naturally incorporates latent processes to capture structured spatial and temporal variability in both the intercept (a) and slope (b) coefficients, while simultaneously accounting for unstructured random effects that absorb site-specific or episodic anomalies. This dual structure enables the model to separate broad-scale climatological patterns from localised factors, enhancing both interpretability and predictive performance.

The use of PC priors for hyperparameters further contributes to model parsimony and interpretability, by penalising overfitting and shrinking unnecessary complexity toward simpler base models. This is particularly important in high-dimensional hierarchical models, where overparameterisation can easily lead to spurious inference.

Taken together, these features make the proposed framework well-suited for solar radiation estimation in data-sparse settings and historical reconstructions, particularly where direct measurements of solar radiation are unavailable or incomplete. The model can also serve as a foundation for further extensions, such as including additional covariates (e.g., satellite-based cloud data or reanalysis variables), modelling daily rather than monthly temporal dynamics, or exploring long-term trends in atmospheric transmissivity in the context of climate variability and change.

Several approaches could be explored to address this issue. One possibility is to explicitly model the censoring effect introduced by threshold-based sunshine duration instruments, either by incorporating a measurement error framework or by introducing a latent continuous representation of n^*. Alternatively, additional covariates such as cloud fraction, visibility, humidity, or precipitation could be integrated to improve radiation estimates under cloudy conditions. A further refinement would involve using a mixture model or zero-inflated approach to handle the overcast regime differently from clear-sky conditions. Modifying the error structure to allow for heteroskedasticity, or incorporating latent indicators for overcast conditions, may also help improve model flexibility. Lastly, increasing the temporal resolution of random effects to the daily scale, possibly using dynamic modelling approaches, could better capture short-term atmospheric variability.

5. Conclusion

This study provides a flexible and scalable approach for estimating solar radiation in regions with sparse direct observations, grounded in physical understanding and supported by modern Bayesian inference tools. The insights gained into spatial, seasonal, and long-term patterns in atmospheric transmissivity highlight the value of combining empirical models with structured statistical frameworks. This methodology offers a solid foundation for future extensions and practical applications in climate, energy, and environmental research.

In particular, when the Angström–Prescott model is embedded in a hierarchical Bayesian spatio-temporal framework, it yields accurate estimates of relative solar radiation (R^*) using sunshine duration (n^*) as the primary predictor. By incorporating structured latent fields, the model successfully captures spatial and seasonal variability, revealing clear, interpretable gradients linked to regional atmospheric conditions. Elevation is found to exert a significant positive influence on the slope coefficient (b), thereby enhancing the sensitivity of radiation to sunshine duration at higher altitudes. Moreover, long-term temporal changes in the slope component suggest possible trends in atmospheric transmissivity, likely driven by shifts in aerosol loading, pollution control measures, or evolving cloud dynamics. Finally, we note that limitations in sunshine duration measurements — especially the zero-inflated nature of n^* due to instrument thresholds — affect model performance under overcast conditions, leading to underdispersion in predicted low-radiation values.

CRediT authorship contribution statement

Santiago Beguería: Writing – original draft, Software, Methodology, Funding acquisition, Formal analysis, Conceptualization. **Sergio M. Vicente-Serrano:** Writing – review & editing, Project administration, Funding acquisition, Conceptualization. **José Manuel Gutiérrez-Llorente:** Writing – review & editing, Project administration, Funding acquisition. **Swen Brands:** Writing – review & editing. **Marcos Gil-Guallar:** Writing – review & editing, Investigation, Data curation. **Alejandro Royo-Aranda:** Writing – review & editing, Investigation,

Data curation. **María del Mar Rondón-Velasco:** Writing – review & editing, Investigation. **Antonio Torralba-Gallego:** Writing – review & editing, Investigation. **Yolanda Luna:** Writing – review & editing. **Ana Morata:** Writing – review & editing.

Declaration of Generative AI and AI-assisted technologies in the writing process

During the preparation of this work, the authors used various large language models to assist in language review and correction. Following the use of these tools, the authors thoroughly reviewed and edited the content to ensure accuracy and take full responsibility for the final version of the publication.

Funding statement

This research work has been funded by the European Commission – NextGenerationEU (Regulation EU 2020/2094) through CSIC's Interdisciplinary Thematic Platform "Clima (PTI Clima) / Development of Operational Climate Services", and by Aragón Government through grant E02-20R.

Declaration of competing interest

The authors declare that they have no known competing financial interests or personal relationships that could have appeared to influence the work reported in this paper.

References

[1] P. Forster, T. Storelvmo, K. Armour, W. Collins, J.-L. Dufresne, D. Frame, D.J. Lunt, T. Mauritsen, M.D. Palmer, M. Watanabe, M. Wild, H. Zhang, The earth's energy budget, climate feedbacks, and climate sensitivity, in: V. Masson-Delmotte, P. Zhai, A. Pirani, S.L. Connors, C. Péan, S. Berger, N. Caud, Y. Chen, L. Goldfarb, M.I. Gomis, M. Huang, K. Leitzell, E. Lonnoy, J.B.R. Matthews, T.K. Maycock, T. Waterfield, O. Yelek¸ci, R. Yu, B. Zhou (Eds.), Climate Change 2021: The Physical Science Basis. Contribution of Working Group I To the Sixth Assessment Report of the Intergovernmental Panel on Climate Change, Cambridge University Press, Cambridge, United Kingdom and New York, NY, USA, 2021, pp. 923–1054, http://dx.doi.org/10.1017/9781009157896.009.

[2] Richard Müller, Uwe Pfeifroth, Remote sensing of solar surface radiation–a reflection of concepts, applications and input data based on experience with the effective cloud albedo, Atmospheric Meas. Tech. 15 (5) (2022) 1537–1561.

[3] Manajit Sengupta, Aron Habte, Stefan Wilbert, Chris Gueymard, Jan Remund, Best Practices Handbook for the Collection and Use of Solar Resource Data for Solar Energy Applications, third ed., 2021, http://dx.doi.org/10.2172/1778700.

[4] Gerrit Hoogenboom, Contribution of agrometeorology to the simulation of crop production and its applications, Agricult. Forest. Meterol. 103 (1–2) (2000) 137–157.

[5] Yuting Yang, Michael L. Roderick, Hui Guo, Diego G. Miralles, Lu Zhang, Simone Fatichi, Xiangzhong Luo, Yongqiang Zhang, Tim R. McVicar, Zhuoyi Tu, et al., Evapotranspiration on a greening earth, Nat. Rev. Earth & Environ. 4 (9) (2023) 626–641.

[6] H. Yu, Y.J. Kaufman, M. Chin, G. Feingold, L.A. Remer, T.L. Anderson, Yves Balkanski, Nicolas Bellouin, O. Boucher, S. Christopher, et al., A review of measurement-based assessments of the aerosol direct radiative effect and forcing, Atmospheric Chem. Phys. 6 (3) (2006) 613–666.

[7] Gerald Stanhill, Shabtai Cohen, Global dimming: a review of the evidence for a widespread and significant reduction in global radiation with discussion of its probable causes and possible agricultural consequences, Agricult. Forest. Meterol. 107 (4) (2001) 255–278.

[8] A. Sanchez-Lorenzo, J. Calbó, M. Wild, Global and diffuse solar radiation in Spain: Building a homogeneous dataset and assessing their trends, Glob. Planet. Change 100 (2013) 343–352.

[9] A. Ångström, Solar and terrestrial radiation, Q. J. R. Meteorol. Soc. 50 (210) (1924) 121–126.

[10] J.A. Prescott, Evaporation from a water surface in relation to solar radiation, Trans. R. Soc. South Aust. 64 (1940) 114–118.

[11] Richard G. Allen, Luis S. Pereira, Dirk Raes, Martin Smith, Crop evapotranspiration: Guidelines for computing crop water requirements, FAO Irrigation and Drainage Paper, vol. 56, Food and Agriculture Organization of the United Nations, Rome, 1998, URL https://www.fao.org/3/x0490e/x0490e00.htm.

[12] J. Fan, L. Wu, F. Zhang, H. Cai, W. Zeng, X. Wang, H. Zou, Empirical and machine learning models for predicting daily global solar radiation from sunshine duration: A review and case study in China, Renew. Sustain. Energy Rev. 100 (2019) 186–212.

[13] D. Matuszko, Long-term variability in solar radiation in krakow based on measurements of sunshine duration, Int. J. Climatol. 34 (1) (2013) 228–234.

[14] Roya Mousavi, Ali-Akbar Sabziparvar, Safar Marofi, Niaz Pak, Majeid Heidari, Calibration of the angström-prescott solar radiation model for accurate estimation of reference evapotranspiration in the absence of observed solar radiation, Theor. Appl. Climatol. 119 (2013) 43–54, http://dx.doi.org/10.1007/s00704-013-1086-7.

[15] M. Despotović, V. Nedić, D. Despotović, S. Cvetanović, Review and statistical analysis of different global solar radiation sunshine models, Renew. Sustain. Energy Rev. 52 (2015) 1869–1880.

[16] C. Iradukunda, K. Chiteka, Angstrom-prescott type models for predicting solar irradiation for different locations in Zimbabwe, Strojn. vestnik- J. Mech. Eng. 69 (1–2) (2023) 32–48.

[17] U. Joshi, P.M. Shrestha, S. Maharjan, A. Bhattarai, N. Bhattarai, N.P. Chapagain, I.B. Karki, K.N. Poudyal, Estimation of solar insolation and Angstrom-Prescott coefficients using sunshine hours over Nepal, Adv. Meteorol. 2022 (1) (2022) 3593922.

[18] R.C. Srivastava, H. Pandey, Estimating Angstrom-Prescott coefficients for India and developing a correlation between sunshine hours and global solar radiation for India, Int. Sch. Res. Not. 2013 (1) (2013) 403742.

[19] S.C. Nwokolo, S.O. Amadi, A.U. Obiwulu, J.C. Ogbulezie, E.E. Eyibio, Prediction of global solar radiation potential for sustainable and cleaner energy generation using improved angstrom-prescott and gumbel probabilistic models, Clean. Eng. Technol. 6 (2022) 100416.

[20] J.C. Mendonça, A. Dalla Bernardina Garcia, J. Nogueira Franco, Coeficientes de angström-prescott para estimar a radiação solar global em campos dos goytacazes, RJ, Irriga 25 (3) (2020) 481–491.

[21] X. Xia, Y. Pan, X. Zhu, J. Zhang, Monthly calibration and optimization of Ångström-prescott equation coefficients for comprehensive agricultural divisions in China, J. Geogr. Sci. 31 (7) (2021) 997–1014.

[22] J. Almorox, C. Voyant, N. Bailek, A. Kuriqi, J.A. Arnaldo, Total solar irradiance's effect on the performance of empirical models for estimating global solar radiation: An empirical-based review, Energy 236 (2021) 121486.

[23] S. Chen, W. Feng, L. He, W. Xiao, H. Feng, Q. Yu, J. Liu, J. He, Parameterization of the Ångström-prescott formula based on machine learning benefit estimation of reference crop evapotranspiration with missing solar radiation data, Hydrol. Process. 38 (2) (2024) e15091.

[24] O. Kisi, M. Alizamir, S. Trajkovic, J. Shiri, S. Kim, Solar radiation estimation in mediterranean climate by weather variables using a novel Bayesian model averaging and machine learning methods, Neural Process. Lett. 52 (3) (2020) 2297–2318.

[25] H. Jadidi, A. Firouzi, M.A. Rastegar, M. Zandi, Bayesian updating of solar resource data for risk mitigation in project finance, Sol. Energy 207 (2020) 1390–1403.

[26] J. Almorox, C. Hontoria, Global solar radiation estimation using sunshine duration in Spain, Energy Convers. Manage. 45 (9–10) (2004) 1529–1535.

[27] J. Almorox, M. Benito, C. Hontoria, Estimation of monthly Ångström–prescott equation coefficients from measured daily data in Toledo, Spain, Renew. Energy 30 (6) (2005) 931–936.

[28] R. Rom00E1n, J. Bilbao, A. de Miguel, Reconstruction of six decades of daily total solar shortwave irradiation in the iberian peninsula using sunshine duration records, Atmos. Environ. 99 (2014) 41–50.

[29] M. Antón, R. Román, A. Sanchez-Lorenzo, J. Calbó, J.M. Vaquero, Variability analysis of the reconstructed daily global solar radiation under all-sky and cloud-free conditions in madrid during the period 1887-1950, Atmos. Res. 191 (2017) 94–100.

[30] A. Manzano, M.L. Martín, F. Valero, C. Armenta, A single method to estimate the daily global solar radiation from monthly data, Atmos. Res. 166 (2015) 70–82.

[31] Daniel Simpson, Håvard Rue, Andrea Riebler, Tito Martins, Sigrun H. Sørbye, Penalising model component complexity: A principled, practical approach to constructing priors, Statist. Sci. 32 (1) (2017) 1–28, http://dx.doi.org/10.1214/16-STS576.

[32] Håvard Rue, Sara Martino, Nicolas Chopin, Approximate Bayesian inference for latent Gaussian models by using integrated nested Laplace approximations, J. R. Stat. Soc. Ser. B Stat. Methodol. (ISSN: 1369-7412) 71 (2) (2009) 319–392, http://dx.doi.org/10.1111/j.1467-9868.2008.00700.x, arXiv:https://academic.oup.com/jrsssb/article-pdf/71/2/319/49686253/jrsssb_71_2_319.pdf.

[33] Finn Lindgren, Håvard Rue, Bayesian spatial modelling with R-INLA, J. Stat. Softw. 63 (19) (2015) 1–25, http://dx.doi.org/10.18637/jss.v063.i19, URL https://www.jstatsoft.org/index.php/jss/article/view/v063i19.

[34] L. Di Antonio, C. Di Biagio, G. Foret, P. Formenti, G. Siour, J.-F. Doussin, M. Beekmann, Aerosol optical depth climatology from the high-resolution MAIAC product over Europe: differences between major European cities and their surrounding environments, Atmospheric Chem. Phys. 23 (19) (2023) 12455–12475, http://dx.doi.org/10.5194/acp-23-12455-2023.

[35] J. Almorox, J.A. Arnaldo, N. Bailek, P. Martí, Adjustment of the angstrom-prescott equation from Campbell-Stokes and kipp-zonen sunshine measures at different timescales in Spain, Renew. Energy 154 (2020) 337–350.

[36] X. Liu, Y. Xu, X. Zhong, W. Zhang, J.R. Porter, W. Liu, Assessing models for parameters of the Ångström-prescott formula in China, Appl. Energy 96 (2012) 327–338.

[37] R.D. García, E. Cuevas, O.E. García, V.E. Cachorro, P. Pallé, J.J. Bustos, P.M. Romero-Campos, A.M. De Frutos, Reconstruction of global solar radiation time series from 1933 to 2013 at the izaña atmospheric observatory, Atmospheric Meas. Tech. 7 (9) (2014) 3139–3150.

[38] European Environment Agency, Emissions of atmospheric pollutants in Europe, 1980–1996, Technical Report 92000, European Environment Agency, 2000, URL https://www.eea.europa.eu/publications/Topic_report_No_92000/file.

[39] K. Bartoszek, D. Matuszko, J. Soroka, Relationships between cloudiness, aerosol optical thickness, and sunshine duration in Poland, Atmos. Res. 245 (2020) 105097.

[40] V. Manara, M. Brunetti, M. Maugeri, A. Sanchez-Lorenzo, M. Wild, Sunshine duration and global radiation trends in Italy (1959–2013): To what extent do they agree? J. Geophys. Res.: Atmospheres 122 (8) (2017) 4312–4331.